Chapter 4

HgCdTe Mid- and Long-Wave Barrier Infrared Detectors for Higher Operating Temperature Condition

Małgorzata Kopytko and Piotr Martyniuk

Additional information is available at the end of the chapter

http://dx.doi.org/10.5772/63943

Abstract

In the last decade, a new architecture design such as nBn device or unipolar barrier photodiode has been proposed to achieve high operating temperature condition. This idea has also been implemented into HgCdTe ternary material system. In this chapter, we present the status of HgCdTe barrier detectors grown by metalorganic chemical vapor deposition with emphasis on numerical simulations of their properties. The device concept of a specific barrier bandgap architecture integrated with Auger suppression is a proper solution for high operating temperature infrared detectors. The device performance is comparable with state-of-the-art HgCdTe photodiodes.

Theoretical modeling of the HgCdTe barrier detectors has been performed using our original numerical program developed at the Institute of Applied Physics, Military University of Technology (MUT) and the commercially available APSYS platform (Crosslight Inc.). The detector's performance was assessed taking into account a wide spectrum of generation-recombination mechanism: Auger, Shockley-Read-Hall, and tunneling processes.

Keywords: HgCdTe, infrared detectors, barrier infrared detectors, high operating temperature, MOCVD growth

1. Introduction

The importance of infrared (IR) radiation technology results from the prevalence of infrared radiation. Infrared is invisible to the human eye radiant energy emitted by any object at temperature above absolute zero. Of particular importance is the spectrum of objects at temperature close to the average temperature of the Earth. It provides the comprehensive

information about their position in space, temperature, surface properties, as well as information about the chemical composition of the atmosphere through which the radiation is transmitted.

All information carried by the infrared radiation can be read and processed by suitable sensors (detectors) that transform infrared energy into other forms, directly and easy to measure. The sensors used to detect infrared radiation are usually equipped with two types of detectors: thermal detectors and photon detectors.

At present, the technology of the mid- (MWIR, 3–8 μm) and long-wave (LWIR, 8–14 μm) infrared radiation is mainly connected with photon detectors, designed on the basis of complex semiconductor materials, such as mercury cadmium telluride (HgCdTe) or indium gallium arsenide (InGaAs). The incident radiation is absorbed within the material by interaction with electrons, and the detector signal is caused by changes of the electric energy distribution. They exhibit both perfect signal-to-noise performance and a very fast response. But to achieve this, the present photon detectors require cryogenic cooling. Cryogenic cooling creates the cost and inconvenient limitations, especially in civil applications.

Thus, higher operation temperature (HOT) condition is one of the most important research areas in infrared technology. The development of a new detector's architecture has been driven by applications requiring multispectral detection, high-frequency response, high detectivity, small size, low weight and power consumption (SWaP), and finally HOT condition. Significant improvements in the reduction of the dark current leading to HOT condition have been achieved by the suppression of Auger thermal generation [1]. In practice, most of the HgCdTe Auger suppressed photodiodes are based on complex graded gap and doping multilayer structures, complicated to grow in terms of technology. The $P^+\pi N^+$ or $N^+\nu P^+$ device structures with a combination of exclusion (P^+/π or N^+/ν) and extraction (N^+/π or P^+/ν) junctions have demonstrated the suppression of Auger mechanisms by reducing the absorber carrier density below thermal equilibrium in reverse bias condition. A recent strategy to achieve HOT detectors includes simple nBn (B: barrier layer) barrier structures [2].

This chapter exhibits the fundamental properties of HgCdTe semiconductors and relates those material parameters that have successful applications as an IR barrier detector alloy. It presents different barrier HgCdTe structures in terms of dark current. The intent of this chapter is to concentrate on a barrier device approach having the greatest impact on IR industry development today.

2. Fundamental HgCdTe properties

The mercury cadmium telluride ($Hg_{1-x}Cd_xTe$) (MCT) is a practically perfect IR detector material system. Its distinctive position depends on three key features:

- cadmium (Cd) composition-dependent energy bandgap (sensing wavelength can be tuned by varying its alloy composition x over the 1–30 μm range),
- large optical coefficients that enable high quantum efficiency, and

http://dx.doi.org/10.5772/63943

- favorable inherent recombination mechanisms that lead to long carrier lifetime and high operating temperature.

Additionally, extremely small change of lattice constant versus composition makes it possible to grow high-quality layers and heterostructures.

2.1. Energy bandgap

The electrical and optical properties of $Hg_{1-x}Cd_xTe$ are determined by energy gap E_g. Energy gap of this compound ranges from −0.30 eV for semimetallic HgTe goes through 0 eV for approximately Cd composition x = 0.15 and finally up to 1.608 eV for CdTe. A number of expressions approximating E_g dependence on composition and temperature are available at present. The most widely used formula is given by Hansen et al. [3]:

$$E_g(x,T) = -0.302 + 1.93x - 0.81x^2 + 0.832x^3 + 5.35\times10^{-4}T(1-2x) \quad (1)$$

where E_g is the energy gap in eV, T is the temperature in K, and x is the Cd molar composition.

Figure 1 shows the empirical fit of the $Hg_{1-x}Cd_xTe$ bandgap according to Hansen et al. [3] versus the Cd molar composition, x at temperature 77 and 300 K. The cutoff wavelength λ_c, defined as that wavelength at which the response drops to 50% of its peak value, is also plotted.

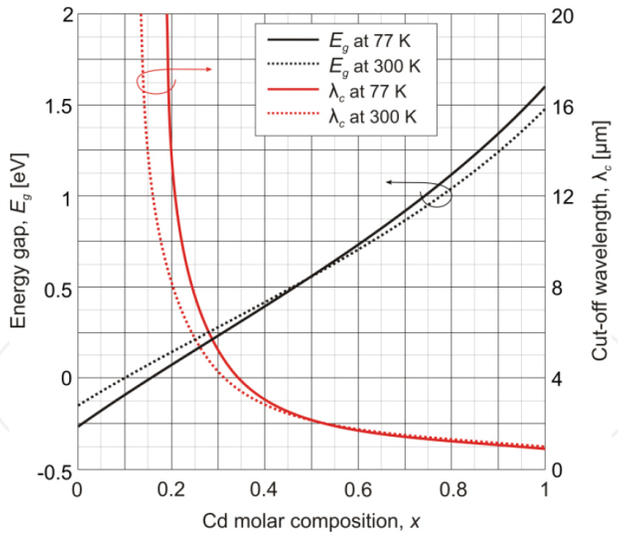

Figure 1. The bandgap structure of $Hg_{1-x}Cd_xTe$ according to Hansen et al. [3] as a function of Cd molar composition, x at temperature of 77 K (solid line) and 300 K (dashed line).

2.2. Electron affinity

For a semiconductor-vacuum interface, electron affinity is defined as the energy obtained by moving an electron from the vacuum just outside the semiconductor to the bottom of the

conduction band just inside the semiconductor. For HgCdTe, electron affinity X can be calculated from [4]:

$$X = 4.23 - 0.813(E_g - 0.083) \tag{2}$$

2.3. Intrinsic concentration

The most widely used expression for intrinsic carrier concentration n_i is that of Hansen and Schmit [5]:

$$n_i = (5.585 - 3.82x + 1.753 \times 10^{-3} T + 1.364 \times 10^{-3}) \times 10^{14} E_g^{3/4} T^{3/2} \exp\left(-\frac{E_g}{2k_B T}\right) \tag{3}$$

where k_B is the Boltzmann constant in eV/K.

The effective mass of electron, m_e, in the narrow gap HgCdTe can be expressed by Weiler's formula that can be approximated by $m_e/m_0 \approx 0.071E_g$, while the effective mass of heavy hole, m_h, is often assumed in modeling of IR detectors according to $m_h = 0.55m_0$.

2.4. Mobility

Due to small effective masses the electron mobility in HgCdTe is high. Mobility Cd molar composition dependence results primarily from the x-dependence of the bandgap and the temperature dependence of the scattering mechanisms. The electron mobility in $Hg_{1-x}Cd_xTe$ in composition range $0.2 < x < 0.6$ and temperature $T > 50$ K can be approximated as [6, 7]

$$\mu_e = \frac{9 \times 10^8 s}{T^{2r}} \tag{4}$$

where μ_e is the electron mobility in m^2/V s, $s = (0.2/x)^{7.5}$, and $r = (0.2/x)^{0.6}$.

For modeling IR HgCdTe photodetectors, the hole mobility is usually calculated assuming that the electron-to-hole mobility ratio, μ_e/μ_h is constant and equal to 100.

2.5. Absorption coefficient

High-quality HgCdTe samples exhibit absorption coefficient α in the short-wavelength region to be in proper agreement with the Kane model. The problems appear to be complicated in the LWIR region by the appearance of an absorption tail extending at energies lower than the energy gap attributed to the composition inhomogeneity. In simulations, a modified Urbach's rule is implemented [8]:

http://dx.doi.org/10.5772/63943

$$\alpha = \alpha_0 \exp\left[\frac{\sigma(E - E_0)}{T + T_0}\right] \tag{5}$$

where α is the absorption coefficient in cm^{-1}, $\alpha_0 = \exp(53.61x - 18.88)$, E is energy in eV, T is the temperature in K, $T_0 = 81.9$ in K, $E_0 = -0.3424 + 1.838x + 0.148x^2$, and $\sigma = 3.267 \times 10^4(1 + x)$.

An empirical formula was thereby employed in the Kane region [9]:

$$\alpha = \alpha_g \exp[\beta(E - E_g)]^{1/2} \tag{6}$$

where the β parameter after Chu et al. [9] is $\beta = -1 + 0.083T + (21 - 0.13T)x$.

2.6. Dielectric constant

The dielectric constants ε are not a linear function of x and temperature dependence was not observed within the experimental resolution. These dependences can be described by the following relations [10]:

$$\varepsilon_\infty = 15.2 - 5.6x + 8.2x^2 \tag{7}$$

$$\varepsilon_S = 20.5 - 15.6x + 5.7x^2 \tag{8}$$

where ε_∞ is the high-frequency dielectric constant and ε_s is the static dielectric constant.

3. Numerical procedure and generation-recombination mechanisms

Theoretical modeling of the HgCdTe barrier detectors has been performed using our original numerical program developed at the Institute of Applied Physics, Military University of Technology (MUT), and the commercially available APSYS platform (Crosslight Inc.). Both programs are based on numerical solution of the Poisson's and the electron/hole current continuity Eqs. (9)–(11) [11, 12]. In addition, both programs include the energy balance Eq. (12):

$$\frac{\partial n}{\partial t} = \frac{1}{q}\nabla \vec{j}_n + G - R \tag{9}$$

$$\frac{\partial p}{\partial t} = -\frac{1}{q}\nabla \vec{j}_p + G - R \tag{10}$$

$$\nabla^2\psi = -\frac{q}{\varepsilon\varepsilon_0}\rho - \frac{1}{\varepsilon}\nabla\psi\nabla\varepsilon \tag{11}$$

$$C_V\frac{\partial T}{\partial t} - H = -\nabla(\chi\cdot\nabla T) \tag{12}$$

where q is the elementary charge, j is the current density, G is the generation rate, and R is the recombination rate. Indices n and p denote electron and hole, respectively. In Poisson's Eq. (11) Ψ is the electrostatic potential and ρ is the electrical charge. In the last term, C_V is the specific heat, χ is the thermal conductivity coefficient, and H is the heat generation term. A Joule heat is introduced as the heat generation in order to include the thermoelectric effect and heat balance.

Current density is usually expressed as functions of quasi-Fermi levels:

$$\vec{j}_n = q\mu_e n\nabla\Phi_n \tag{13}$$

$$\vec{j}_p = q\mu_h p\nabla\Phi_p \tag{14}$$

where Φ_n and Φ_p denote the quasi-Fermi levels.

The difference $G - R$ (Eqs. (9) and (10)) is the net generation of electron-hole pairs and depends on all generation recombination (GR) effects including influence of thermal mechanisms as well as tunneling mechanisms.

Depending on this approach, either two or three important carrier thermal GR processes, Shockley-Read-Hall (SRH), Auger, and radiative mechanisms were included in simulations. A radiative GR process could be ignored because photon recycling restricts the influence of that process on the performance of HgCdTe photodiodes [13, 14]. Tunneling mechanisms were considered due to band-to-band tunneling (BTB) and trap-assisted tunneling (TAT).

Thermal generation could be given as a sum of radiative, Auger 1, Auger 7, and SRH mechanisms. BTB and TAT effects can also be included as a GR process:

$$(G-R) = (G-R)_{RAD} + (G-R)_{AUG} + (G-R)_{SRH} + (G-R)_{BTB} + (G-R)_{TAT} \tag{15}$$

The set of transport Eqs. (9)–(11) is commonly known; however, their solution consists of serious mathematical and numerical problems. The equations are nonlinear, and are complex functions of electrical potential, quasi-Fermi levels, and temperature. The details concerning the solutions of Poisson's equation are presented in Appendix A.

http://dx.doi.org/10.5772/63943

3.1. Radiative process/photon recycling

For a long time, internal radiative GR processes have been considered to be the main fundamental limit to detector performance and the performance of practical devices have been compared to that limit. The following relation can be used to estimate radiative $(G-R)_{RAD}$ contribution [15]:

$$(G-R)_{RAD} = B(np - n_i^2) \tag{16}$$

$$B = 5.9052\times10^{18} n_i^{-2} \varepsilon T^{3/2} \sqrt{\frac{1+x}{(81.9+T)}} \exp\left(-\frac{E_g}{k_B T}\right)(E_g^2 + 3k_B T E_g + 3.75 k_B^2 T^2) \tag{17}$$

Due to photon recycling effect, the radiative lifetime is highly extended. According to Humpreys [13], most of the photons emitted in photodetectors as a result of radiative decay are immediately reabsorbed and the observed radiative lifetime is only a measure of how well photons can escape from the volume of the detector. In many cases, especially in the case of semiconductors with high reflective index, radiative mechanism can be omitted in numerical modeling.

3.2. Auger processes

There are several types of Auger processes, and among them Auger 1 and Auger 7 are the most dominant due to the smallest threshold energies. The Auger 1 generation is the impact ionization by an electron, generating an electron-hole pair and is dominant in n-type material while Auger 7 is the impact generation of electron-hole pair by a light hole and dominates in p-type material.

The Auger generation and recombination rates strongly depend on temperature via the dependence of carrier concentration and intrinsic time on temperature. Therefore, cooling is a natural and a very effective way to suppress Auger processes according to the following relation [16]:

$$(G-A)_{AUG} = (C_n n + C_p p)(np - n_i^2) \tag{18}$$

$$\begin{aligned} C_n = {} & 5\times10^{-22} \mid F_1 F_2 \mid \left[\left(\frac{E_g}{k_B T}\right)^3 \exp\left(1+2\frac{m_e^*}{m_h^*}\right)\left(\frac{E_g}{k_B T(m_e^*/m_h^*)}\right)\right]^{-1/2} \\ & \times n_i^{-2}[3.8\times10^{-18}\varepsilon^2\left(\frac{1}{m_e^*}\right)\cdot\left(1+2\frac{m_e^*}{m_h^*}\right)\sqrt{1+\frac{m_e^*}{m_h^*}}]^{-1} \end{aligned} \tag{19}$$

$$C_p = \gamma \cdot C_n \tag{20}$$

where $|F_1F_2|$ is the overlap integrals for Bloch functions. The ratio γ has been calculated as a function of composition and temperature and is assumed to be ranging from 3 to 60 depending on temperature [17, 18].

3.3. Shockley-Read-Hall processes

The Shockley-Read-Hall (SRH) mechanism is not an intrinsic process because it occurs via levels in the forbidden energy gap. Metal site vacancies (mercury vacancies) are considered as an SRH centers in HgCdTe. The reported position of SRH centers for both n- and p-type material is assumed as 1/3 E_g or 3/4 E_g from the conduction band. The $(G-R)_{SRH}$ rate could be calculated according to the following formula [19–21]:

$$(G-R)_{SRH} = \frac{np - n_i^2}{\tau_{p0}(n_0 + n_1) + \tau_{n0}(p_0 + p_1)} \tag{21}$$

where

$$n_1 = n_i \exp\left(\frac{E_T - E_{Fi}}{k_B T}\right) \tag{22}$$

$$p_1 = n_i \exp\left(\frac{E_{Fi} - E_T}{k_B T}\right) \tag{23}$$

n_1 and p_1 mean concentrations in the case in which the trap level E_T coincides with the Fermi level E_{Fi}. The terms $\tau_{n0} = (c_n N_T)^{-1}$ and $\tau_{p0} = (c_p N_T)^{-1}$ are the shortest possible time constants for the electron and hole capture coefficients (c_n and c_p), respectively. N_T denotes the mercury vacancy concentration.

3.4. Tunneling processes

BTB tunneling is calculated as a function of the applied electric field F [22–24]:

$$(G-R)_{BTB} = \frac{qFm^*}{2\pi^2\hbar^3} P_0 \overline{E} \tag{24}$$

where $\hbar$ is the reduced Planck constant and m^* is the electron effective mass related to the tunneling mechanism defined as

http://dx.doi.org/10.5772/63943

$$m^* = \frac{m_c m_v}{m_c + m_v} \tag{25}$$

where m_c and m_v are the effective masses in conduction and valence bands, respectively.

Tunneling probability P_0 with a zero perpendicular (to the x-direction) momentum can be estimated using the following relations:

$$P_0 = \exp\left(\frac{\pi (m^*)^{1/2} E_g^{3/2}}{2\sqrt{2} qF\hbar}\right) \tag{26}$$

$$\overline{E} = \frac{\sqrt{2} qF\hbar}{2\pi (m^*)^{1/2} E_g^{1/2}} \tag{27}$$

where $\overline{E}$ is a measure of significance of perpendicular momentum range. In other words, tunneling probability decreases with increasing value of $\overline{E}$. If is $\overline{E}$ small, the only electrons with perpendicular momentum near zero can tunnel through the energy barrier. Typically $\overline{E}$ is in a range of 5–100 meV.

TAT contribution was estimated according to formula similar to the SRH process described by Eq. (21) [25]. However, the trapping rate strongly depends on the ionization energy E_T; the electric field can essentially influence τ_{n0} and τ_{p0} values that are inversely proportional to trapping rates. This means that the electric field enhances a GR process around the mercury vacancy by decreasing the energy required both for the emission of an electron with energy level E_T to the conduction band as well as for the emission of a hole with the empty level E_T to the valence band. Taking into account this mechanism, the c_n and c_p parameters are modified. For this purpose, Eq. (21) is modified with δ_n and δ_p parameters that determine the relative changes in the size of the emission factors of electrons and holes caused by the effects associated with the electric field. The TAT effect expressed by GR process is

$$(G-R)_{TAT} = \frac{np - n_i^2}{\frac{\tau_{p0}}{\delta_p}(n_0 + n_1) + \frac{\tau_{n0}}{\delta_n}(p_0 + p_1)} \tag{28}$$

4. HgCdTe barrier detectors—principle of operation for higher operating temperatures

The introduction of unipolar barrier in various photovoltaic configurations causes a drastic change in architecture and the principle of operation of IR detectors. The idea of unipolar

barrier infrared detector (BIRD) implies that barriers can block one carrier type (electron or hole) but allow the unimpeded flow of the other. Assuming that Simple BIRD nB_nn detector can be concluded as a hybrid of a photoconductor and a photodiode. The nB_nn detector looks like a photodiode in a part except that the junction (space charge region) is replaced by a unipolar barrier (B_n: n-type doped barrier layer) blocking the electrons, whereas p-contact is replaced by the n-contact. The nB_nn detector is nearly lacking the depletion region in an active layer, which leads to the reduction of SRH contribution to the net dark current. In low temperatures (below the crossover temperature), the nB_nn detector should exhibit a higher signal-to-noise ratio in comparison with a conventional *p-n* photodiode operating at the same temperature and should operate at a higher temperature with the same dark current.

The idea of the nB_nn detector was proposed for bulk III-V materials; however, its introduction to the second type of superlattices has allowed the implementation of the concept of nB_nn with a greater control of arrangement of optimal band structure. Contrary to III-V materials, uniformly n-type-doped HgCdTe does not exhibit valence band offset (VBO) ≈ 0 eV between the absorber and the barrier (e.g., MWIR HgCdTe − VBO < 200 meV depending on both the absorber/barrier composition and doping, T = 200 K), which is a key limiting detector performance [26]. Depending on the wavelength of operation, a relatively high bias (so-called "turn on" voltage) is required to be applied to the device to collect the photogenerated carriers. This leads to strong BTB and TAT effects due to a high electric field at the barrier-absorber heterojunction.

Proper p-type doping at the cap barrier and barrier absorber heterojunctions should lower VBO in HgCdTe. However, p-type doping is the technological challenge posed by dopant activation after molecular beam epitaxy (MBE) growth. Metalorganic chemical vapor deposition (MOCVD) technology is considered more favorable, which allows both *in situ* donor and acceptor doping. It seems to be more attractive in terms of the growth of pB_pn and pB_pp (B_p: p-type barrier) HgCdTe barrier structures. Barrier structures with p-type-doped constituent layers grown by MOCVD were presented by Kopytko et al. [27, 28].

5. Numerical simulations of barrier detectors

Theoretical modeling of the HgCdTe barrier detectors has been performed using our original numerical program developed at the Institute of Applied Physics, Military University of Technology (MUT) and the commercially available APSYS platform (Crosslight Inc.). Both programs are based on numerical solution of the Poisson's and the electron/hole current continuity Eqs. (9)–(11). In addition, both programs include the energy balance Eq. (12).

In simulations, we chose HgCdTe barrier detectors with different 50% cutoff wavelengths up to 3.6 μm (MWIR) and 9 μm (LWIR) at 230 K. MWIR devices were investigated by using our original numerical program, while LWIR device was investigated by the APSYS platform. **Table 1** presents selected parameters applied in the numerical modeling of MWIR HgCdTe barrier detectors.

http://dx.doi.org/10.5772/63943

	MWIR (own program)	LWIR (APSYS)
Trap concentration, N_T (cm^{-3})	1.5×10^{-7}	10^{14}
Trap ionization energy, E_T	$3/4E_g$	$1/3E_g$
Trap capture coefficient, c_n, c_p ($cm^3\ s^{-1}$)	1.5×10^{-7}, 3×10^{-9}	
Dislocations density, G_{DIS} (cm^{-2})	10^6	–
Dislocations ionization energy, E_{DIS}	$0.32E_g$	–
Dislocations capture coefficient, c_n, c_p ($cm^3\ s^{-1}$)	3×10^{-7}, 6×10^{-8}	–
Overlap matrix F_1F_2	0.3	

Table 1. Parameters taken in modeling of MWIR and LWIR HgCdTe barrier detectors.

5.1. Design and fabrications of HgCdTe barrier detectors

The epitaxial structures were grown by MOCVD. Generally, the analyzed MWIR $p^+B_pnN^+$ and $p^+B_ppN^+$ (a capital letter denotes wider band; the symbol "+" denotes strong doping) structures consists of four HgCdTe layers: p^+-B_p cap-barrier structural unit (highly doped with arsenic p-type cap contact layer and p-type wide bandgap barrier), intentionally undoped (due to donor background concentration with n-type conductivity) or low p-type-doped absorption layer and wide bandgap highly doped N^+ bottom contact layer. In the LWIR $n^+p^+B_ppN^+$ device, the cap contact is a combination of highly doped n- and p-type layers. Such design should create a tunneling junction to allow collection of photogenerated holes. Moreover, the cap n^+ layer provides low-resistance ohmic contact. **Figure 2** shows the considered MWIR and LWIR HgCdTe heterostructure with parameters assumed for the growth and modeling.

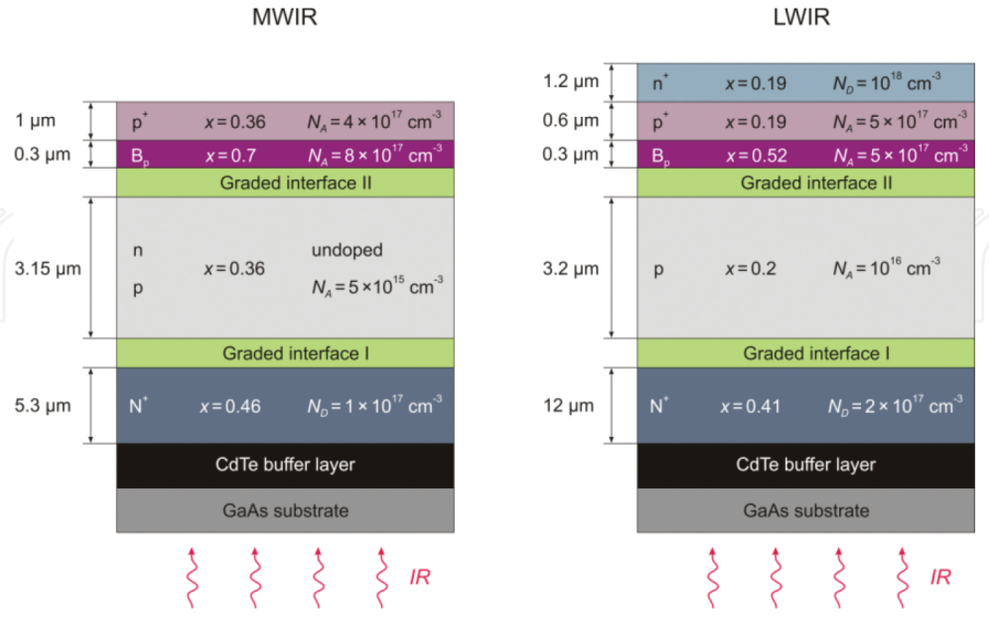

Figure 2. MWIR and LWIR HgCdTe heterostructure with parameters assumed for the growth and modeling. x is the alloy composition, N_A is the acceptor concentration, and N_B is the donor concentration.

5.2. MWIR HgCdTe barrier detectors

Our original numerical program incorporates HgCdTe electrical properties to estimate MWIR device performance taking into account Auger, SRH, as well as BTB and TAT tunneling mechanisms. Two types of SRH centers were included in the model: metal site vacancies and dislocation related centers [29, 30]. The two types of centers are characterized by different ionization energies and capture coefficients (**Table 1**).

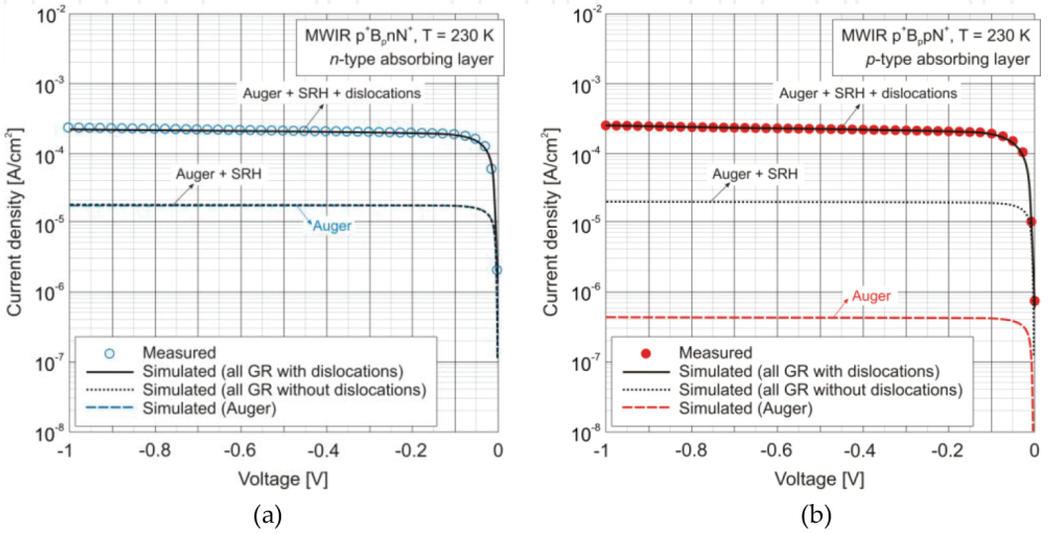

Figure 3. Measured current-voltage characteristics for MWIR HgCdTe (a) $p^+B_pnN^+$ and (b) $p^+B_pPN^+$ barrier detectors operated at 230 K. The experimental data are compared to the theoretical prediction considering overall GR effect and Auger processes.

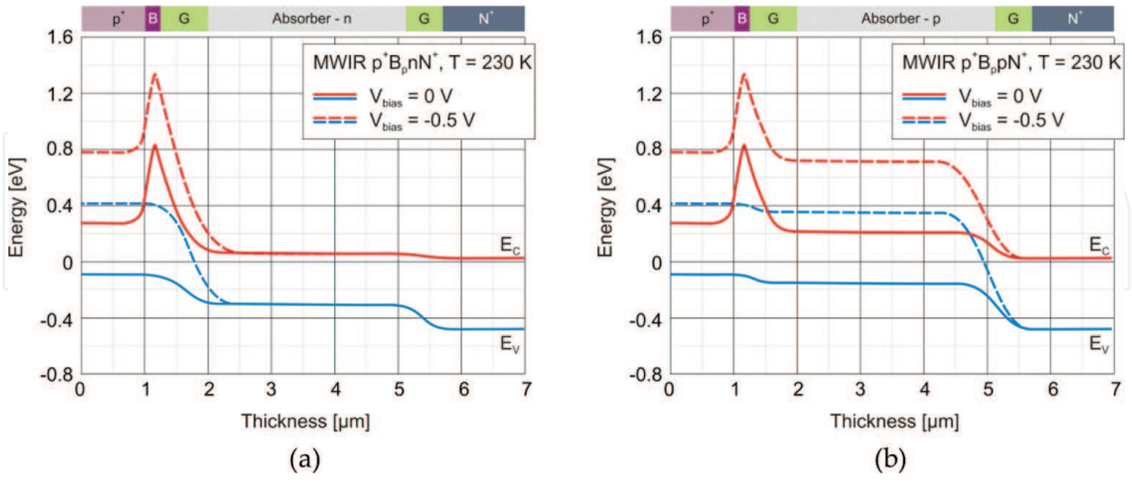

Figure 4. Simulated band diagram for MWIR HgCdTe (a) $p^+B_pnN^+$ and (b) $p^+B_pPN^+$ photodetectors operated at 230 K, unbiased, and under 0.5 V reverse bias.

Figure 3 presents an example of simulated fitting characteristics of MWIR HgCdTe barrier detectors at a temperature of 230 K. The calculations were made taking into account all

http://dx.doi.org/10.5772/63943

considered mechanisms of thermal generation, tunneling, and impact ionization. As we can see, in a wide region of bias voltages, an excellent agreement has been obtained between the experimental and calculated results. What is more, the Auger and the SRH parts of the dark current are clearly visible. The SRH GR process was calculated both for dislocation-free structures and structures containing misfit dislocations. In both types of detectors, the SRH mechanism associated with misfit dislocations has an impact on the dark currents.

Figure 4 presents the calculated bandgap diagrams of the simulated structures for unbiased and under 0.5 V reverse bias. As expected, the p-type doping of the barrier, with controlled interdiffusion process, and *x*-graded region at the barrier and absorber interfaces introduce a zero offset in the valence band. Bandgap diagrams under reverse bias clearly idicates that in the $p^+B_pnN^+$ device a decisive heterojunction is at the barrier and absorber interface while in the $p^+B_pnN^+$ photodiode at the absorber and highly doped bottom contact layer.

Dislocation-free structures should provide one order of magnitude lower dark currents. For the device with an n-type absorbing layer, saturated dark current is limited by Auger mechanisms. In the case of good-quality p-type HgCdTe, with a reduced number of a structural defect, the influence of exclusion and extraction effects might be more effective than in the n-type material due to a larger diffusion length of electrons than holes. It is apparent that Auger 1 mechanism prevails over Auger 7 mechanism and determines the minority carrier lifetime in intrinsic, n-type, and low-doped p-type materials.

5.3. LWIR HgCdTe barrier detectors

The commercially available APSYS platform (Crosslight Inc.) was implemented for LWIR device simulation procedures. The applied model incorporates HgCdTe electrical properties to estimate device performance taking into account Auger, SRH, as well as BTB and TAT tunneling mechanisms.

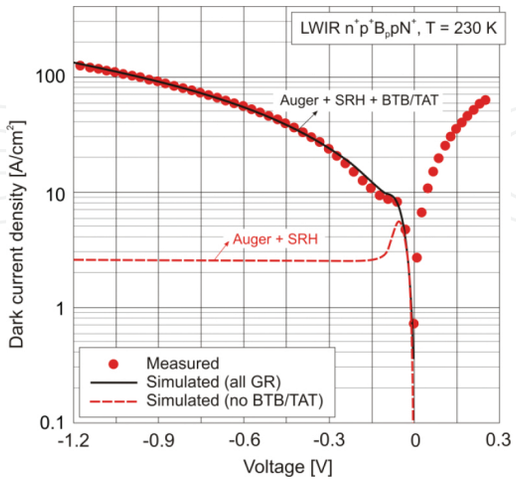

Figure 5. Measured current-voltage characteristics for the LWIR HgCdTe $n^+p^+B_pN^+$ barrier photodiode operated at 230 K. The experimental data are compared to the theoretical prediction considering Auger, SRH, and BTB/TAT mechanisms.

The measured and calculated dark current characteristics of the LWIR HgCdTe $n^+p^+B_ppN^+$ photodiode are presented in **Figure 5**. It is shown that the most effective current transport mechanism in the LWIR HgCdTe barrier photodiode are tunneling effects at the decisive heterojunctions (especially TAT). **Figure 6** presents the calculated bandgap diagrams of the simulated structures for unbiased and under –0.5 V bias. Bandgap diagrams under reverse bias clearly idicates that the tunneling mechanism occurs at the absorber and highly doped bottom contact heterojunction.

Tunneling between trap centers and valence and conduction bands are main reasons of increasing SRH processes with the increasing reverse bias voltage. In contrast to our numerical program, the APSYS platform does not distinguish trap centers between metal site vacancies and dislocation-related centers. The best fit of experimental data with theoretical predictions has been obtained for the trap density (N_T) assumed at the level of 10^{14} cm^{-3} with ionization energy (E_T) counted from the conduction at $1/3E_g$. In TAT simulation, the Hurkx et al. model was implemented [24].

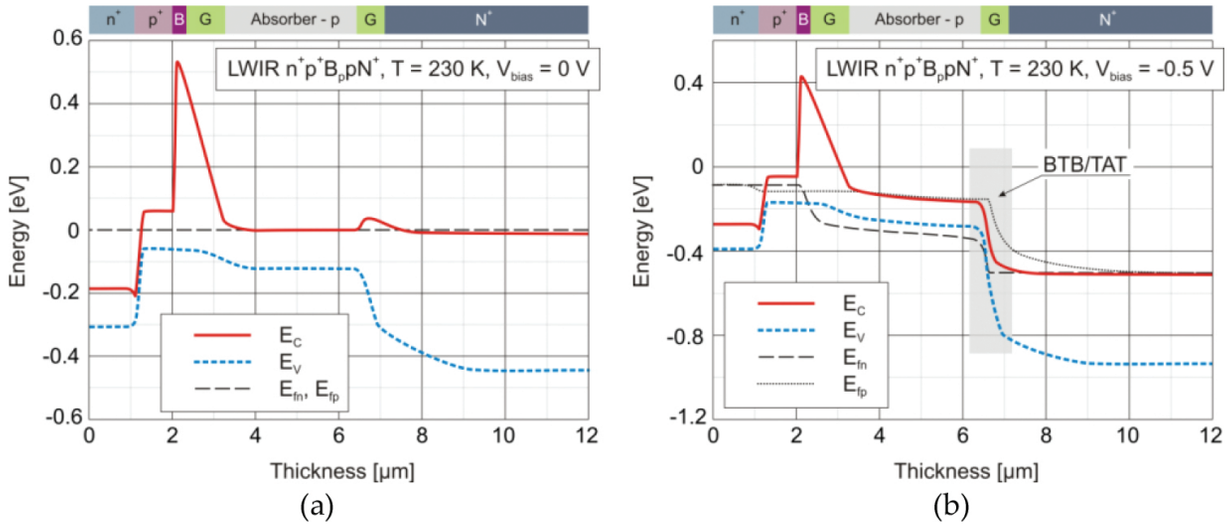

Figure 6. Simulated band diagram for the LWIR HgCdTe $n^+p^+B_ppN^+$ photodiode operated at 230 K: (a) unbiased and (b) under 0.5 V reverse bias.

Dominant SRH process override Auger supression due to the exclusion and extraction effect. For a low reverse biases, up to the threshold voltage (–60 mV), an increase in the dark current is observed. In this voltage region, the differential resistance increases and at the final stage becomes infinite. Above the threshold voltage, the dark current decreases (the current-voltage characteristics exhibits a negative differential resistance) reaching the minimum value.

Under reverse bias, the electrons are extracted from the absorber region by positive electrode connected to a bottom N^+-layer. The electrons are also excluded from the absorber near the barrier layer. The energy barrier between the cap layer and absorber regions blocks the electron flow from the cap layer. As a consequence, the hole concentration also decreases. The exclusion effect is limited by the level of acceptor concentration (electrical carrier neutrality), as well as by thermal generation that restores the thermal equilibrium state.

http://dx.doi.org/10.5772/63943

6. Summary

The current-voltage characteristics of MWIR and LWIR HgCdTe barrier detectors operating with Peltier cooling were investigated by computer simulations confronted with experimental data. Two numerical programs—our original program developed at the Institute of Applied Physics, Military University of Technology (MUT) and the commercially available APSYS platform (Crosslight Inc.)—have been used for modeling. Both programs are based on numerical solution of commonly known Poisson's and electron/hole current continuity equations. The applied model incorporates HgCdTe electrical properties to estimate device performance taking into account Auger, SRH, as well as BTB and TAT tunneling mechanisms. Due to reabsorption of photons generated by carrier recombination, also called the photon recycling, the radiative recombination is not assumed to limit the performance of HgCdTe photodetectors and was omitted in the simulations.

Typically, reverse biased infrared detectors are characterized by diffusion and tunnel-like dark current. At low reverse biases, the diffusion dark current is mainly limited by the Auger and SRH processes. At higher voltages, field-enhanced TAT via traps located at dislocation cores as well as mercury vacancies seems to be the most important mechanism of dark current generation, especially in the LWIR device. This mechanism is significant at the p-N^+ interface, characterized by a large electric field.

The architecture of the LWIR $n^+p^+B_ppN^+$ photodiode needs to be optimized to reduce the tunneling mechanisms at the p-N^+ heterojunction. Numerical analysis is a proper tool to indicate the fields of improving device performances. For example, one possibility to reduce TAT is tuning of composition at interfaces aimed to locate highly dislocated region at a wider gap part of the p-N^+ transition region where they have little effect on the dark current.

Numerical calculations have been performed for the structures of HgCdTe; however, the models may also be generalized for other semiconductor materials.

Acknowledgements

The work has been carried out under the financial support of the Polish National Science Centre as research Projects Nos. DEC-2013/08/M/ST7/00913 and DEC-2013/08/A/ST5/00773.

Appendices

Appendix A

Numerical solution of transport equations for semiconductor devices

The numerical method applied in this study employs Newton's algorithm to obtain a steady-state solution to the set of transport Eqs. (9)–(11) using an initial distribution of the electrostatic

potential in thermodynamic equilibrium that is obtained from conditions of electrical neutrality. Poisson's equation under equilibrium conditions gives the first solution function in the iterative procedure that leads to the solution of the set of transport equations under nonequilibrium conditions.

First, we have to solve the Poison's equation in steady-state conditions. If the charge density in the semiconductor structure does not depend on the gradient of the potential, the Poisson's Eq. (11) can be represented in the following form:

$$\varepsilon\varepsilon_0\nabla^2\psi + \varepsilon_0\nabla\psi\nabla\varepsilon + q\rho = 0 \tag{A1}$$

where

$$\rho = p - n + N_D^+ - N_A^- \tag{A2}$$

is the difference between the density of positive and negative charge carriers (the hole concentrations p plus the concentration of ionized donors N_D^+ minus the electron concentrations n and the concentration of ionized acceptors N_A^-).

To find the numerical solution of the nonlinear Poisson Eq. (A1) by using a diffusion-equation differential scheme, we replaced it by an equivalent diffusion equation as it was postulated in reference [31]:

$$\frac{\partial\psi}{\partial t} = \varepsilon\varepsilon_0\nabla^2\psi + \varepsilon_0\nabla\psi\nabla\varepsilon + q\rho \tag{A3}$$

where t is the pseudotime.

The initial values of the electrostatic potential ψ^0 at every point of the semiconductor structure can be numerically calculated assuming the electrical neutrality conditions. It is expressed by an equation of electrical neutrality:

$$p(\psi) - n(\psi) + N_D^+(\psi) - N_A^-(\psi) = 0 \tag{A4}$$

The concentration of ionized acceptors and donors are expressed as

$$N_A^- = \frac{N_A}{1 + a\exp[(E_A - E_{Fi})/k_BT]} \tag{A5}$$

http://dx.doi.org/10.5772/63943

$$N_D^+ = \frac{N_D}{1 + b\exp[(E_{Fi} - E_D)/k_B T]} \tag{A6}$$

where E_A and E_D are the ionization energies of acceptors and donors, respectively.

Then, an iterative approach should be used to solve the set of transport Eqs. (9)–(11). Let us bring an iterative algorithm to solve Poisson's equation which was presented in reference [31]. Eq. (A1) may be expressed in the following form:

$$L(\psi) = 0 \tag{A7}$$

The iterative form of Eq. (A7) can be expressed as follows:

$$L(\psi^{n+1}) = L(\psi^n) + \frac{\partial L(\psi^n)}{\partial \psi^n}\delta\psi^{n+1} \tag{A8}$$

where Ψ^{n+1} is a vector of $n + 1$ iterative correction of vector Ψ. Similarly, Eq. (A3) can be expressed as

$$\frac{\partial \psi}{\partial t} = L(\psi) \tag{A9}$$

and the iterative form of Eq. (A9) can be expressed as

$$\delta\psi^{n+1} = \Delta t L(\psi^n) + \frac{1}{2}\Delta t \frac{\partial L(\psi^n)}{\partial \psi^n}\delta\psi^{n+1} \tag{A10}$$

where Δt is the pseudotime step.

An iteration method allows the calculation of corrections to electrical potential, quasi-Fermi levels, and temperature [32]:

$$\Psi = \Psi^0 + \delta\Psi,\ \Phi_n = \Phi_n^0 + \delta\Phi_n,\ \Phi_p = \Phi_p^0 + \delta\Phi_p,\ T = T^0 + \delta T \tag{A11}$$

and consequently to other physical parameters:

$$n = n^0 + \frac{\partial n}{\partial \psi}\delta\psi + \frac{\partial n}{\partial \Phi_n}\delta\Phi_n + \frac{\partial n}{\partial T}\delta T \tag{A12}$$

$$p = p^0 + \frac{\partial p}{\partial \psi}\delta\psi + \frac{\partial p}{\partial \Phi_p}\delta\Phi_p + \frac{\partial p}{\partial T}\delta T \tag{A13}$$

$$G - R = G^0 - R^0 + \delta(G - R) \tag{A14}$$

where

$$\begin{aligned}\delta(G-R) = &\frac{\partial(G-R)}{\partial n}\left(\frac{\partial n}{\partial \psi}\delta\psi + \frac{\partial n}{\partial \Phi_n}\delta\Phi_n + \frac{\partial n}{\partial T}\delta T\right) \\ &+ \frac{\partial(G-R)}{\partial p}\left(\frac{\partial p}{\partial \psi}\delta\psi + \frac{\partial p}{\partial \Phi_p}\delta\Phi_n + \frac{\partial p}{\partial T}\delta T\right)\end{aligned} \tag{A15}$$

Finally, knowing the electric potential Ψ, the electron affinity X, and the bandgap energy E_g, we can determine the energy values for the edge of the conduction and valence bands:

$$E_C = -X - q\psi \tag{A16}$$

$$E_V = -X - q\psi - E_g \tag{A17}$$

Author details

Małgorzata Kopytko* and Piotr Martyniuk

*Address all correspondence to: malgorzata.kopytko@wat.edu.pl

Institute of Applied Physics, Military University of Technology, Warsaw, Poland

References

[1] T. Ashley and C. T. Elliott, "Nonequlibrium devices for infra-red detection," Electron. Lett. 21, 451–452 (1985).

[2] S. Maimon and G. Wicks, "nBn detector, an infrared detector with reduced dark current and higher operating temperature," Appl. Phys. Lett. 89, 151109 (2006).

[3] G. L. Hansen, J. L. Schmidt and T. N. Casselman, "Energy gap versus alloy composition and temperature in $Hg_{1-x}Cd_xTe$," J. Appl. Phys. 53, 7099 (1982).

[4] J. Wenus, J. Rutkowski and A. Rogalski, "Two-dimensional analysis of double-layer heterojunction HgCdTe photodiodes," IEEE Trans. Electron Dev. 48, 1326–1332 (2001).

[5] G. L. Hansen and J. L. Schmit, "Calculation of intrinsic carrier concentration in $Hg_{1-x}Cd_xTe$," J. Appl. Phys. 54, 1639–1640 (1983).

[6] J. P. Rosbeck, R. E. Star, S. L. Price and K. J. Riley, "Background and temperature dependent current–voltage characteristics of $Hg_{1-x}Cd_xTe$ photodiodes," J. Appl. Phys. 53, 6430–6440 (1982).

[7] W. Scott, "Electron mobility in $Hg_{1-x}Cd_xTe$," J. Appl. Phys. 43, 1055–1062 (1972).

[8] E. Finkman and S. E. Schacham, "The exponential optical absorption band tail of $Hg_{1-x}Cd_xTe$," J. Appl. Phys. 56, 2896–2900 (1984).

[9] J. Chu, B. Li, K. Liu and D. Tang, "Empirical rule of intrinsic absorption spectroscopy in $Hg_{1-x}Cd_xTe$," J. Appl. Phys. 75, 1234–1235 (1994).

[10] R. Dornhaus, G. Nimtz and B. Schlicht, "Narrow-gap semiconductors," Springer, Berlin (1983).

[11] W. van Roosbroeck, "Theory of the electrons and holes in germanium and other semiconductors," Bell Syst. Tech. J. 29, 560–607 (1950).

[12] M. Kurata, "Numerical analysis of semiconductor devices," Lexington Books, DC Heath (1982).

[13] R. G. Humpreys, "Radiative lifetime in semiconductors for infrared detectors," Infrared Phys. Technol. 26, 337–342 (1986).

[14] K. Jóźwikowski, M. Kopytko and A. Rogalski, "Numerical estimation of carrier generation-recombination processes and photon recycling effect in 3-μm n-on-p HgCdTe photodiodes," Opt. Eng. 50, 061000-1–061000-8 (2011).

[15] W.van Roosbroeck and W. Shockley, "Photon-radiative recombination of electrons and holes in germanium," Phys. Rev. 94, 1558–1560 (1954).

[16] A. R. Beattie and P. T. Landsberg, "Auger effect in semiconductors," Proc. R. Soc. Lond. A 249, 16–28 (1959).

[17] M. A. Kinch, F. Agariden, D. Chandra, P.-K. Liao, H. F. Schaake and H. D. Shih, "Minority carrier lifetime in p-HgCdTe," J. Electron. Mater. 34, 880 (2005).

[18] S. Krishnamurthy and T. N. Casselman, "A detailed calculation of the Auger lifetime in *p*-type HgCdTe," J. Electron. Mater. 29, 828–831 (2000).

[19] W. Shockley and W. T. Read, "Statistics of recombinations of holes and electrons," Phys. Rev. 87, 835–842 (1952).

[20] R. N. Hall, "Electron-hole recombination in germanium," Phys. Rev. 87, 387 (1952).

[21] R. Kiran, "Optimization of the $Hg_{1-x}Cd_xTe$ surface and its characterization by electrical and optical techniques," Ph.D. dissertation, University of Illinois at Chicago, Chicago, IL (2008).

[22] E. O. Kane, "Zener tunneling in semiconductors," Phys. Chem. Solids 2, 181–188 (1960).

[23] C. B. Duke, "Tunneling in Solids," volume 10 of Solid state physics: advances in research and applications," Academic Press, New York (1969).

[24] J. L. Moll, "Physics of semiconductors," chapter 12, McGraw-Hill, New York (1964).

[25] G. A. Hurkx, D.B.M. Klaassen and M. P. G. Knuvers, "A new recombination model for device simulation including tunneling," IEEE Trans. Electron Dev. 39(2), 331 (1992).

[26] A. M. Itsuno, J. D. Phillips and S. Velicu, "Mid-wave infrared HgCdTe nBn photodetector," Appl. Phys. Lett. 100, 161102 (2012).

[27] M. Kopytko, "Design and modeling of high-operating temperature MWIR HgCdTe nBn detector with *n*- and *p*-type barriers," Infrared Phys. Technol. 64, 47–55 (2014).

[28] M. Kopytko, K. Jóźwikowski and A. Rogalski, "Fundamental limits of MWIR HgCdTe barrier detectors operating under non-equilibrium mode," Solid-State Electron. 100, 20–26 (2014).

[29] K. Jóźwikowski, M. Kopytko, J. Piotrowski, A. Jóźwikowska, Z. Orman and A. Rogalski, "Near-room temperature MWIR HgCdTe photodiodes limited by vacancies and dislocations related to Shockley–Read–Hall centres," Solid-State Electron. 66(1), 8–13 (2011).

[30] K. Jóźwikowski, A. Jóźwikowska, A. Rogalski and L. R. Jaroszewicz, "Simplified model of dislocations as a SRH recombination channel in the HgCdTe heterostructures," Infrared Phys. Technol. 55(1), 98–107 (2012).

[31] A. Jóźwikowska, "Numerical solution of the nonlinear Poisson equation for semiconductor devices by application of a diffusion-equation finite difference scheme," J. Appl. Phys. 104, 063715 (2008).

[32] A. Jóźwikowska, K. Jóźwikowski, J. Rutkowski and A. Rogalski, "Generation-recombination effects in high temperature HgCdTe heterostructure photodiodes," Opto-Electron. Rev. 12(4), 417–428 (2004).